Journal of the European Ceramic Society 46 (2026) 117735

Contents lists available at ScienceDirect

Journal of the European Ceramic Society

journal homepage: www.elsevier.com/locate/jeurceramsoc

Precipitation hardening in lead-free $Na_{0.5}Bi_{0.5}Ti0_3$-$BaTiO_3$

Sabrina Kahse [a,b,*], Siegfried Teuber [a], Tanja Einhellinger-Müller [b], Friederike Aßmann [b], Florian Schönhöfer [b], Sebastian Zischke [c], Lovro Fulanovic [a], Jürgen Rödel [a]

[a] Division of Nonmetallic-Inorganic Materials, Department of Materials and Earth Sciences, Technical University of Darmstadt, 64287 Darmstadt, Germany
[b] CeramTec GmbH, 91207 Lauf an der Pegnitz, Germany
[c] Central Facility for Electron Microscopy, RWTH Aachen University, 52062 Aachen, Germany

ARTICLE INFO

Keywords:
Piezoceramics
Lead-free
$Na_{0.5}Bi_{0.5}TiO_3$-$BaTiO_3$
Precipitation hardening
Ferroelectric hardening

ABSTRACT

Ferroelectric hardening is indispensable for piezoelectrics used in high-power applications, as it enhances their performance by avoiding thermal and dielectric breakdowns. Recently, precipitation hardening has been introduced as a promising strategy, where intragranular precipitates, formed by an aging treatment, can effectively pin domain walls and improve piezoelectric properties. In this work, the lead-free ternary system $Na_{0.5}Ba_{0.5}TiO_3$-$BaTiO_3$-$MgTiO_3$ is investigated for its potential to form precipitates. The substitution of NBT-BT with $MgTiO_3$ leads to a 200 % increase in mechanical quality factor due to intergranular secondary phase hardening. Scanning and transmission electron microscopy confirm the formation of additional intragranular precipitates by an aging treatment. Electromechanical characterization indicates a strong link between precipitation during aging and the enhancement of coercive field by 19 % and mechanical quality factor by 30 %, followed by a reduction in polarization. Lower aging temperature promotes the formation of smaller-sized precipitates and thereby impact the electromechanical behavior.

1. Introduction

Hard ferroelectric materials are crucial for high-power applications, such as piezoelectric transducers, ultrasonic motors, and welders [1]. Operating near resonance frequencies, the performance is significantly impacted by energy losses, leading to heat generation and, ultimately, degradation of material properties over time [2–4]. In ferroelectrics, domain wall motion is a primary source of mechanical losses [5]. The mechanical quality factor Q_m serves as an indicator of these losses, being inversely proportional to them [2,3]. Ferroelectric hardening plays a key role in minimizing these losses by reducing domain wall motion, leading to enhanced Q_m [6,7]. Hard $Pb(Zr,Ti)O_3$ (PZT) is commonly used in these applications due to its outstanding electromechanical properties such as a high Q_m as well as piezoelectric coefficient d_{33} [2,8]. However, due to increasing environmental concerns over lead toxicity and related regulations, the demand towards lead-free ferroelectrics has intensified [9].

Relaxor-ferroelectric $(1\text{-}x)Na_{0.5}Bi_{0.5}TiO_3$-$xBaTiO_3$ (NBT-BT) solid solutions have been discussed as one of the most promising candidates to substitute lead-based piezoceramics [10,11], as it exhibits exceptional stability of the electromechanical properties over a broad vibration velocity range. It even outperforms PZT at vibration velocities higher than 1 m/s [12–14]. At the morphotropic phase boundary (6–7 mol% of $BaTiO_3$) both rhombohedral and tetragonal phase coexist, leading to a peak of piezoelectric coefficient at d_{33}= 125–167 pC/N [10,15]. However, the low ferroelectric-relaxor transition temperature $T_{F\text{-}R}$ at about 100 °C [16,17], and the overall low electromechanical quality factor Q_m of 150 limits the use in applications [14].

To tailor NBT-BT piezoceramics for enhanced performance in high-power applications, ferroelectric hardening becomes essential. The state-of-the-art approach is acceptor doping, which leads to an increase in the concentration of oxygen vacancies that form dopant-vacancy defect dipoles. These defect dipoles immobilize domain walls and consequently improve Q_m [3,18,19]. Secondary phase ferroelectric hardening via 0–3 ceramic-ceramic composite is also reported to be an effective hardening approach [20,21]. It has the specific advantage in comparison to elemental doping at elevated temperatures, as the hardening effect remains more stable [22]. For NBT-BT:ZnO composite, it is reported that the hardening mechanism is driven by mechanical mismatch stresses that develop between the matrix and inclusions to pin

* Corresponding author at: Division of Nonmetallic-Inorganic Materials, Department of Materials and Earth Sciences, Technical University of Darmstadt, 64287 Darmstadt, Germany.
E-mail address: kahse@ceramics.tu-darmstadt.de (S. Kahse).

https://doi.org/10.1016/j.jeurceramsoc.2025.117735
Received 13 May 2025; Received in revised form 27 July 2025; Accepted 4 August 2025
Available online 5 August 2025

domain walls effectively. These stresses arise after cooling down the composite from the sintering temperature due to differences in thermal expansion between the matrix and inclusions. Additionally, the application of an electric field further intensifies these stresses as the ferroelectric NBT-6BT matrix undergoes phase transition and domain switching, while the non-ferroelectric ZnO inclusions remain unaffected [23,24]. This method effectively hinders domain wall motion, leading to an improvement in both the depolarization temperature and Q_m [25].

Recently, precipitation hardening emerged as a new concept for ferroelectric hardening. In systems such as $BaTiO_3$-$CaTiO_3$ and Li-doped $NaNbO_3$, intragranular coherent precipitates are formed through an annealing treatment, the so-called aging, of a supersaturated solid solution, obtained by a quenching procedure. Those precipitates are reported to effectively inhibit domain wall motion by inducing misfit strains between precipitates and matrix [26,27]. This mechanism offers a distinct advantage over the composite approach, as intragranular precipitates prevail closer to domain walls than the intergranular inclusions in composites, enhancing the pinning interaction.

Until now, precipitation hardening has been applied only on ferroelectrics. In contrast, NBT-BT is a relaxor, which undergoes an irreversible relaxor-ferroelectric transition upon applying an external field [11,28]. Relaxors are known to react sensitively to changes in composition, leading to reduced depolarization temperatures [29–31]. This sensitivity presents challenges in identifying an appropriate composition where precipitation hardening can be effectively applied.

This work explores precipitation hardening in lead-free ternary solid solution NBT-BT-$MgTiO_3$ as potential ferroelectric hardening approach in NBT-BT, aiming to improve its characteristic low Q_m. Although achieving full solubility of $MgTiO_3$ in NBT-BT matrix presents a challenge, aging treatments applied to quenched samples facilitate the formation of Mg-rich intragranular precipitates. Microstructural and electrical characterization indicate a strong link between precipitation during aging and the significant enhancement of coercive field and Q_m, alongside a reduction in polarization. The aging temperature notably influences the extent of precipitation and, consequently, the electrical properties of the material, highlighting its importance in optimizing the hardening method.

2. Experimental

The ternary composition $0.96(0.94Na_{0.5}Bi_{0.5}TiO_3\text{-}0.06BaTiO_3)\text{-}0.04MgTiO_3$ (NBT-6BT-4$MgTiO_3$) was prepared via conventional solid-state synthesis. Precursor powders of Na_2CO_3 (99.98 %), Bi_2O_3 (99.975 %), $BaCO_3$ (99.85 %), anatase-TiO_2 (99.6 %) and MgO (99.99 %) were utilized (all from Alfa Aesar GmbH & Co. KG, Germany). After stochiometric weighing, the powders were planetary milled in a 500 ml nylon milling container with 3 mm yttria-stabilized zirconia balls in ethanol for 21 h at 250 rpm and dried afterward at 105 °C. The homogenized powder was then calcined at 830°C for 3 h using heating and cooling rates of 5 K/min and ball-milled again with the same conditions. Disk-shaped samples with 10 mm diameter and 1.5 mm height were first pressed under 40 MPa uniaxial pressure, followed by cold isostatic pressing (KIP 100 E, Weber-Pressen, Germany) with 350 MPa. The green bodies were sintered in a closed alumina crucible containing sacrificial powder at 1100 °C for 2 h in a tube furnace (R50/500/12, Nabertherm, Germany). Subsequently, from the sintering temperature, the samples were air-quenched using a conventional fan, achieving an average cooling rate of 180 K/min. The quenching process was employed to kinetically suppress the formation of secondary phases that may arise from reduced solubility with decreasing temperature. These quenched samples were annealed at temperatures below the sintering temperature to control the formation of precipitates. This annealing treatment is denoted as aging in the following. Aging was conducted at 600 °C and 800 °C for 24 h with 5 K/min heating and cooling rates, to assess the influence of aging temperature on precipitate formation. The precipitation hardening treatment is illustrated in Fig. 1, highlighting the expected microstructure after quenching and aging.

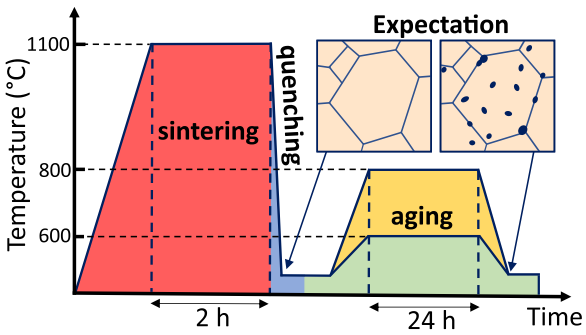

Fig. 1. Scheme of the heat treatment for precipitation hardening, including the microstructural expectation after each step.

Thermogravimetric analysis (TGA), differential thermal analysis (DTA), and evolved gas analysis (EGA) using mass spectroscopy were conducted to investigate changes in the calcination process by the substitution with $MgTiO_3$. For TGA and DTA measurements, homogenized mixtures of precursors of pure NBT-6BT and NBT-6BT-4$MgTiO_3$ were heated with a rate of 5 K/min up to 1000 °C in flowing air at a rate of 50 ml/min and 10 ml/min of argon as protective gas in a STA449C Jupiter (Netzsch Gerätebau GmbH, Selb, Germany). The outgassing species from decomposition were simultaneously analyzed with a heated transfer line operated at 200 °C to the STA by QMS403C Aëolos Quadro mass spectrometer (Netzsch Gerätebau GmbH, Selb, Germany). The following mass-to-charge signals (m/z) as quasi multi-ion detection (QMID) were utilized: $m/z = 18$ (H_2O^+) and 44 (CO_2^+). All measurements were adjusted to account for buoyancy.

Ex-situ X-ray diffraction (XRD) (Cu $K_{\alpha1}/K_{\alpha2}$; D8, Bruker Corporation, Germany) was used to investigate the phase evolution during calcination. Homogenized mixtures of precursors of NBT-6BT-4$MgTiO_3$ were heated to 600 °C, 700 °C, 750 °C, 800 °C, and 850 °C with a rate of 5 K/min and subsequently air-quenched when the temperature was reached.

Structural analysis of quenched and aged samples was conducted by XRD in Bragg-Brentano geometry (D8, Bruker Corporation, Germany) with Cu $K_{\alpha1}/K_{\alpha2}$ radiation. Bulk samples were crushed to powder, followed by annealing at 400 °C for 1 h to remove crushing-induced strains. The 2Θ range of 10° to 70° with a step size of 0.02° was used for all XRD measurements.

Microstructural analysis was performed on a 0.25 µm polished sample surface by means of scanning electron microscopy (SEM, JSM-7600F, Jeol, Tokyo, Japan). The backscattered electron (BSE) detector, a working distance of 8.0 mm, and an electron energy of 8 kV were used. SEM micrographs were analyzed regarding the volume fraction and average size of the Mg-rich secondary phase particles via area analysis (V_V=A_A). To evaluate changes in their distribution due to aging, the particle density was defined as the number of Mg-rich secondary phase particles per unit area. Two approaches were employed. For the total density of Mg-rich secondary phase, both intergranular and intragranular particles were counted and related to the investigated area. Comparable areas of approximately 670 μm^2 were analyzed across all samples to ensure consistency and allow for reliable comparison of the results. The specific density of intragranular precipitates was determined by using the number of particles inside grains divided by the area of the investigated grains, which included more than 100 individual grains. For both methods, a minimum of three micrographs per sample were used for statistical evaluation. Additionally, average grain size was determined on thermally etched samples. Grain size measurements were acquired from at least three micrographs with a minimum of 100 grains from different positions for each sample. For all microstructural analyses, ImageJ was used to determine either the area or Feret diameter of the secondary phase particles or grains, respectively.

High-resolution microstructure imaging and elemental mapping

were conducted using transmission electron microscopy (TEM) (JEM-F200, Jeol, Tokyo, Japan) and energy dispersive spectroscopy (EDX). TEM samples were prepared via focused ion beam (FIB) milling (Crossbeam 350 FIB/SEM, Zeiss, Germany).

For electrical measurements, disk-shaped samples were ground to a thickness of 0.6 mm, followed by sputtering of silver electrodes onto the surfaces. The samples were then annealed at 400°C for 1 h to relieve residual stresses introduced by the grinding process. Polarization and strain hysteresis loops were recorded with a Sawyer-Tower circuit (reference capacitor 10 μF) and an optical strain sensor (Philtec Inc., United States). A bipolar triangular wave of 7 kV/mm and 1 Hz was used to reach saturation. Samples were DC poled at 6 kV/mm for 5 min for small signal properties. The d_{33} was measured by a Berlincourt-meter (PiezoMeter System PM300, Piezotest Pte Ltd., Singapore) with a driving frequency of 110 Hz, static clamping force of 2 N and dynamic driving force of 0.25 N. Mechanical quality factor (Q_m) was quantified by the 3 dB calculation method according to standards EN 50324 [32] using an impedance analyzer (Alpha-Analyzer, Novocontrol technologies GmbH, Germany) at 10 mV. T_{F-R} was determined from temperature-dependent dielectric permittivity measurement on poled samples using an LCR-Meter (4284 A Precision LCR-Meter, Hewlett Packard, United States) and a chamber furnace (LE6/11/3216, Nabertherm, Germany) with a heating rate of 2 K/min and 1 V_{RMS} probing signal at 1 kHz.

3. Results and discussion

3.1. Processing

Precipitation requires a material system that exhibits a complete solubility of a dopant in the matrix at the solid solution temperature and a decreasing solubility with decreasing temperature, in order to form precipitates by an aging treatment of a quenched sample [33,34]. Hence, phase diagrams are of particular importance when selecting a material system. In case of NBT-BT-based systems such phase diagrams are missing, to the best of our knowledge. This study investigates $MgTiO_3$-substituted NBT-6BT, a composition selected through empirical evaluation for precipitation hardening. The selection has been based on comparing the Goldschmidt tolerance factor t and ionic radii of the solute and matrix composition, which may provide insights into structural compatibility within the perovskite lattice [35]. A model system $LiNbO_3$-$NaNbO_3$ (LN-NN) serves as a guideline for selection, [27], where ilmenite $LiNbO_3$ (LN) precipitates have been formed by aging treatment to pin domain walls successfully. As LN has a tolerance factor of 0.92, it is hypothesized that if the solute composition has a tolerance factor between 0.9 and 0.95, the solubility in NBT-6BT (t = 1) may be comparable to LN in NN (t = 0.97) system. $MgTiO_3$ has a tolerance factor of 0.9 and is therefore considered a suitable candidate to dissolve in NBT-6BT, while also exhibiting reduced solubility as the temperature decreases, as seen in the LN-NN system. The smaller ionic radius of Mg^{2+} (120 pm in 12-fold coordination) compared to Na^+ (139 pm) and Bi^{3+} (145 pm) suggests that Mg^{2+} can potentially occupy the A-site of perovskite structure such as Li^+ (125 pm) in NN system [36]. According to Goldschmidt [35], if the ionic radius of the substitute differs by 15 %, full solubility can be reached, while if it differs by 15–30 % limited solubility can occur. Hence, a limited solubility may be present in the $MgTiO_3$-substituted NBT-BT composition. The fact that $MgTiO_3$ crystallizes in the ilmenite structure, similar to LN, makes it an appealing solute composition. A further advantage of this dopant lies in the fact that Mg has limited solubility in NBT-BT and leads to considerable hardening [17,37,38]. In case that not all of the $MgTiO_3$ could dissolve in the matrix, residual MgO may have a beneficial effect in terms of secondary phase hardening through misfit-induced stresses, as reported for NBT-6BT:ZnO composite [20]. If $MgTiO_3$ precipitates in NBT-BT, these precipitates may potentially have an analogous domain pinning effect as LN in NN, enhancing the mechanical quality factor by ferroelectric hardening.

Chemical substitution can modify the solid-state reactions due to changes in the thermodynamics of the system. To assess the impact of $MgTiO_3$ substitution on the solid-state reaction during calcination, simultaneous thermal analysis combined with gas evolution measurements are performed and compared to unmodified NBT-6BT, which is presented in Fig. 2. DTA reveals three endothermic peaks. The first can be attributed to the evaporation of adsorbed atmospheric water, supported by the strong water signal in the EGA and the initial mass loss of 1.2 % observed for the $MgTiO_3$-substituted sample. A similar response is observed in unmodified NBT-6BT, but less pronounced, likely due to less exposure to atmospheric moisture. The subsequent two endothermic peaks in the DTA curve at around 600 °C and 800 °C can be associated with the formation of NBT-BT, as both compositions exhibit similar decomposition of carbonates and thermal features. Between 500 °C and 850 °C, both samples show a mass loss of approximately 5.5 %, which is in good agreement to the theoretical CO_2 loss, calculated from their stochiometric mixture. The peak observed at 800 °C appears broadened for the $MgTiO_3$-substitued composition. Since $MgTiO_3$ is reported to calcine in the range of 800 °C to 900 °C [39,40], its thermal response may overlap with that of NBT-BT, potentially contributing to the observed DTA peak broadening. However, the data remain inconclusive regarding whether $MgTiO_3$ forms a separate phase or is incorporated into NBT-BT matrix. Overall, the substitution of $MgTiO_3$ does not appear to significantly alter the calcination behavior.

Ex-situ XRD has been conducted to investigate evolution of crystal structures during calcination and to complement the thermal analysis and thereby addressing the limitations of DTA and enhancing the understanding of the solid-state reactions in NBT-6BT-4$MgTiO_3$. Fig. 3 displays the ex-situ XRD pattern for uncalcined homogenized powder and calcined powder from 600 °C up to 850 °C. The uncalcined XRD pattern is a superposition of the XRD pattern of the precursor powders of γ-Na_2CO_3 (#95549), Bi_2O_3 (#15752), $BaCO_3$ (#137395), anatase-TiO_2 (#9852) and MgO (#9863). Reference reflections from ICSD database for precursor powders, $BaTiO_3$ (#15453) and NBT-6BT (#230436) are depicted in Fig. 3(b) to relate changes in the XRD pattern with reactions of the precursor powders [41]. At 600 °C the solid-state reaction of the NBT-based perovskite structure initiates, indicated by a reflex starting to form at $2\Theta \approx 32.5°$, which can be assigned to the (110) reflex of the perovskite structure [42,43]. Hou *et al.* [43] reported the onset formation of the NBT-xBT perovskite structure at 600°C. In their in-situ XRD study, a continuous transformation of the Bi_2O_3 ($2\bar{1}1$) to perovskite

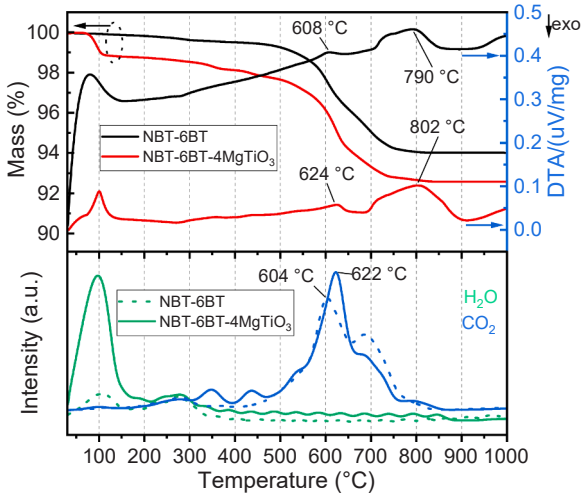

Fig. 2. Simultaneous thermal analysis and gas evolution measurements of the homogenized mixture of precursors of pure thermal analysis (b) evolved gas analysis by using mass spectroscopy with mass-to-charge signals of H_2O, CO and CO_2.

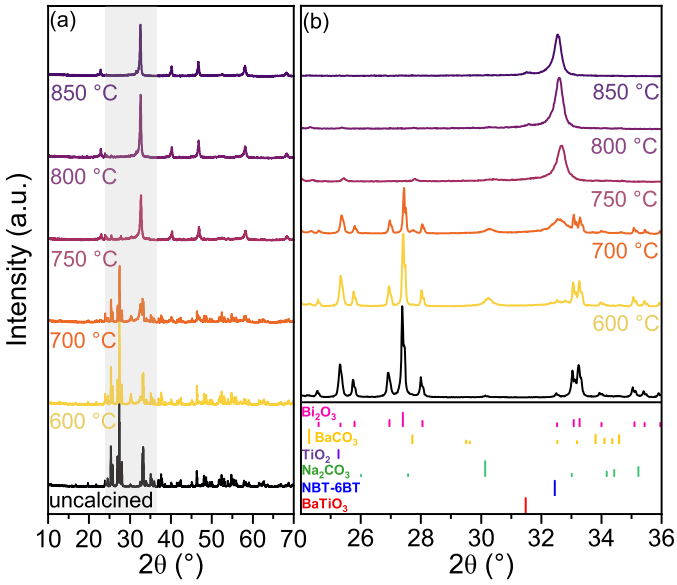

Fig. 3. XRD of the uncalcined NBT-BT-4$MgTiO_3$ powder heated with 5 K/min to different temperatures and subsequently quenched in air is depicted in (a) for the full range and in (b) for a detailed diffractogram. Possible phases are indicated by tick marks, which represent the reflections of the respective phase with their length being proportional to the intensity of reflections according to the crystallographic database [41].

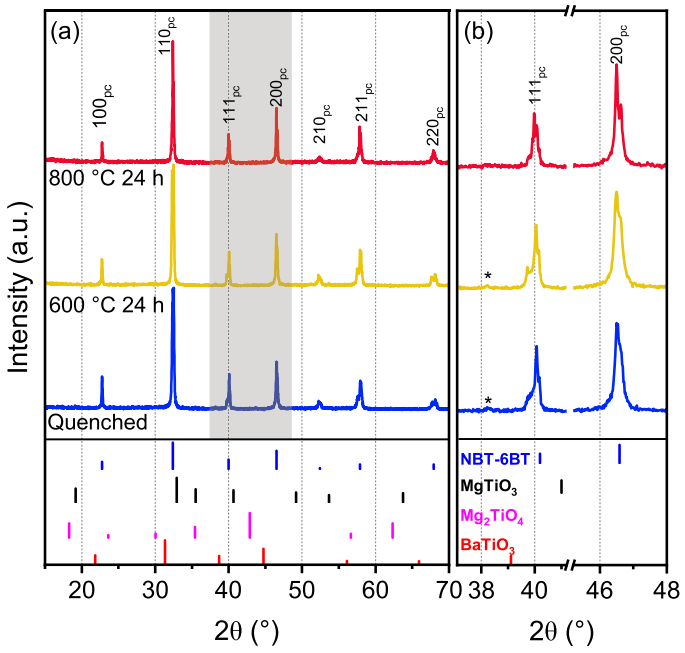

Fig. 4. (a) Normalized x-ray diffractogram of quenched (blue), aged samples at 600 °C for 24 h (yellow) and 800 °C for 24 h (red), where reflections of possible secondary phases are represented by tick marks according to the crystallographic database (length is proportional to the intensity of reflections) [41]. (b) 111 $_{pc}$ and 200 $_{pc}$ reflections are presented with greater detail. The superlattice reflex (SR) of the rhombohedral structure is indicated by *.

(110) reflex has been observed, supporting the particle conversion mechanism proposed by Aksel *et al.* [44]. In this mechanism, Bi_2O_3 serves as a host for a diffusion-driven process, where Na_2CO_3 and TiO_2 precursors gradually integrate into Bi_2O_3. The strong CO_2 release, observed at around 622 °C in the thermal analysis, can therefore be attributed to the start of Na_2CO_3 diffusion into Bi_2O_3 followed by its reaction. This aligns with the previously reported onset temperature of 600 °C for pure NBT-BT formation [43]. This suggests that $MgTiO_3$--substitution does not significantly alter the start temperature for the calcination reaction.

Despite Na_2CO_3 and Bi_2O_3 react at 600 °C, the γ-Na_2CO_3 reflex at 2Θ≈ 30.1° does not seem to vanish at temperatures up to 800 °C. This may be due to the formation of an intermediate $Bi_4Ti_3O_{12}$ phase, which has its strongest reflex as well at 2Θ≈ 30.1° (ICSD #16488). Hou *et al.* suggest the presence of this intermediate phase between 600 °C and 800 °C during the processing of NBT-xBT [43]. Others have also reported the formation of this phase at that temperature range [44,45]. Na_2CO_3 persists in four polymorphs (α, β, γ, and δ), each transitioning at different temperatures [46,47]. Up to 350 °C, the room temperature stable monoclinic γ-phase transforms into the β-phase, followed by a transition to the α-phase between 350 °C to 500 °C. In the temperature range of 300 °C to 500 °C, the minor release of CO_2 is likely associated with the polymorphic transitions Na_2CO_3 and its partial decomposition [43]. Due to the overlap of α-Na_2CO_3 with stronger Bi_2O_3 reflections, it is challenging to trace changes in Na_2CO_3 during calcination, complicating efforts to directly correlate CO_2 evolution with specific reaction stages. [43,48].

At 850 °C, calcination appears to be complete, as no reflections from precursor phases are detected. Alongside the perovskite (110) reflex at 2Θ≈ 32.5°, a minor reflex is visible at 2Θ≈ 31.5°. This most likely corresponds to $BaTiO_3$-phase, as reported in literature [43]. They propose that this formation is preferred due to increased interaction between TiO_2 and $BaCO_3$ particles by inhomogeneous local distribution. After sintering, this reflection is no longer visible, implying that $BaTiO_3$ is completely incorporated into the matrix during the high-temperature thermal process (Fig. 4).

No reflections corresponding to $MgTiO_3$ is observed, which may indicate its incorporation in NBT-BT matrix. Note that this can also be attributed to the detection limit of the XRD technique. Overall, $MgTiO_3$ substitution does not seem to influence the reaction pathway of the NBT-BT processing, as it is complementary to the one reported by Hou *et al.* [43].

3.2. Structure

Structural differences between potential precipitated phases and the perovskite NBT-BT enable the identification of the presence of precipitates in post-aging treatment via XRD with Cu $K_{α1}/K_{α2}$ radiation. Fig. 4 displays the diffraction patterns of quenched and two differently aged samples alongside reference reflection from the ICSD database of possible phases (NBT-6BT #230436, $MgTiO_3$ #55285, Mg_2TiO_4 #65793, $BaTiO_3$ #15453) [41]. Both quenched and aged samples exhibit perovskite structure with no detectable reflection attributable to secondary phases in the aged samples. This absence does not necessarily indicate that no precipitates have formed by the aging treatment. Instead, it implies that the quantity of any secondary phase may be below the XRD detection limit [49]. Additionally, the highest intense reflections of the ilmenite-structured $MgTiO_3$ and perovskite-structured $BaTiO_3$ overlap with the 110 $_{pc}$ reflex of NBT-6BT, possibly making it harder to identify minor phases. Consequently, qualitative XRD analysis alone does not confirm the presence of precipitates formed during the aging process.

Analysis of the quenched sample reveals splitting in the 111 $_{pc}$ reflex, evidenced by a shoulder at lower 2Θ values, along with a weak superlattice reflex (SR) characteristic of R3c symmetry at 2Θ≈ 38.3° (Fig. 4 (b)) [50,51]. Given that the 200 $_{pc}$ reflex appears as a singlet, it is an indication that the quenched sample exhibits a pseudocubic phase with some rhombohedral symmetry. Wohninsland *et al.* reported that quenching NBT-6BT samples promotes an enhanced rhombohedral distortion, while furnace-cooled samples only exhibit a pseudocubic structure [52]. Such enhanced lattice distortion implies the stabilization of the ferroelectric long-range order upon quenching [52,53]. This has

been linked to the Bi^{3+}-off-centering along the 111-direction by quenching [54]. Another explanation has been proposed, involving an increase in oxygen vacancy concentration upon quenching [53]. For the sample aged at 600 °C for 24 h, a similar diffraction pattern to the quenched sample is observed, indicating that aging treatment does not revert the quenching-induced ferroelectric order. In contrast, the sample aged at 800 °C for 24 h reveals neither the SR nor a distinct shoulder on the 111 $_{pc}$ reflex, and no splitting of the 200 $_{pc}$ reflex into 002 and 200 reflections. This absence of splitting indicates that the sample exhibits only a pseudocubic structure. This observation signifies that the quenching-induced distortion is reversed during the aging at 800 °C. It aligns with the report of the removal of the quenching effect when annealed in air at 800 °C for 12 h [55].

The microstructural analysis of the quenched sample was conducted using SEM and TEM (Fig. 5). It reveals the presence of secondary phases not detected by XRD analysis. EDX spectroscopy identifies these secondary phases as Mg-rich and Ba-rich regions. In BSE micrographs, the secondary phases can be distinguished both by contrast and morphology; Ba-rich phases appear brighter due to the higher atomic mass of Ba compared to Mg, while Mg-rich regions exhibit a darker contrast. Morphologically, Mg-rich phases are predominantly round, while Ba-rich phases demonstrate more angular shapes. Liu *et al.* observed Ba- and Ti-rich secondary phases in 1.5 mol% Mg-doped NBT-BT, implying that Mg doping promotes the liquid phase formation, leading to inhomogeneous diffusion of elements [37]. In contrast, Ba-rich phases may form due to partial Mg occupancy at the B-site. This causes elemental non-stoichiometry at both the B-site and A-site, resulting in the formation of a Ba- and Ti-rich phases.

Contrary to expectations of having a supersaturated single phase after quenching [33,34], results indicate that Mg and Ba have not been completely dissolved in the matrix at the sintering temperature. This means the solubility limit is reached. However, assuming the solubility of $MgTiO_3$ decreases with temperature, precipitate formation may occur as a result of the aging treatment.

Fig. 6 presents bright-field TEM images of both quenched and aged samples. In quenched samples, Mg- and Ba-rich phases are predominantly found in intergranular regions, as confirmed by EDX evaluation. Aging promotes an increase of Mg-rich secondary phases, which are observed both within the grains and along grain boundaries. Notably, the sample aged at 600 °C for 24 h exhibits a higher concentration of intragranular Mg-rich phase compared to the sample aged at 800°C.

Given the fact that TEM provides highly localized information, SEM has been employed to assess the volume fraction, average size, and density of both Mg-rich intergranular and intragranular secondary phases (Fig. 7). Especially information on the formation of precipitates inside the grain is crucial for improved domain pinning and, thus, for the hardening effect, which is given by the density of intragranular precipitates. The BSE contrast allowed clear differentiation between Mg-rich and Ba-rich secondary phases, thereby enabling investigation of their evolution upon aging.

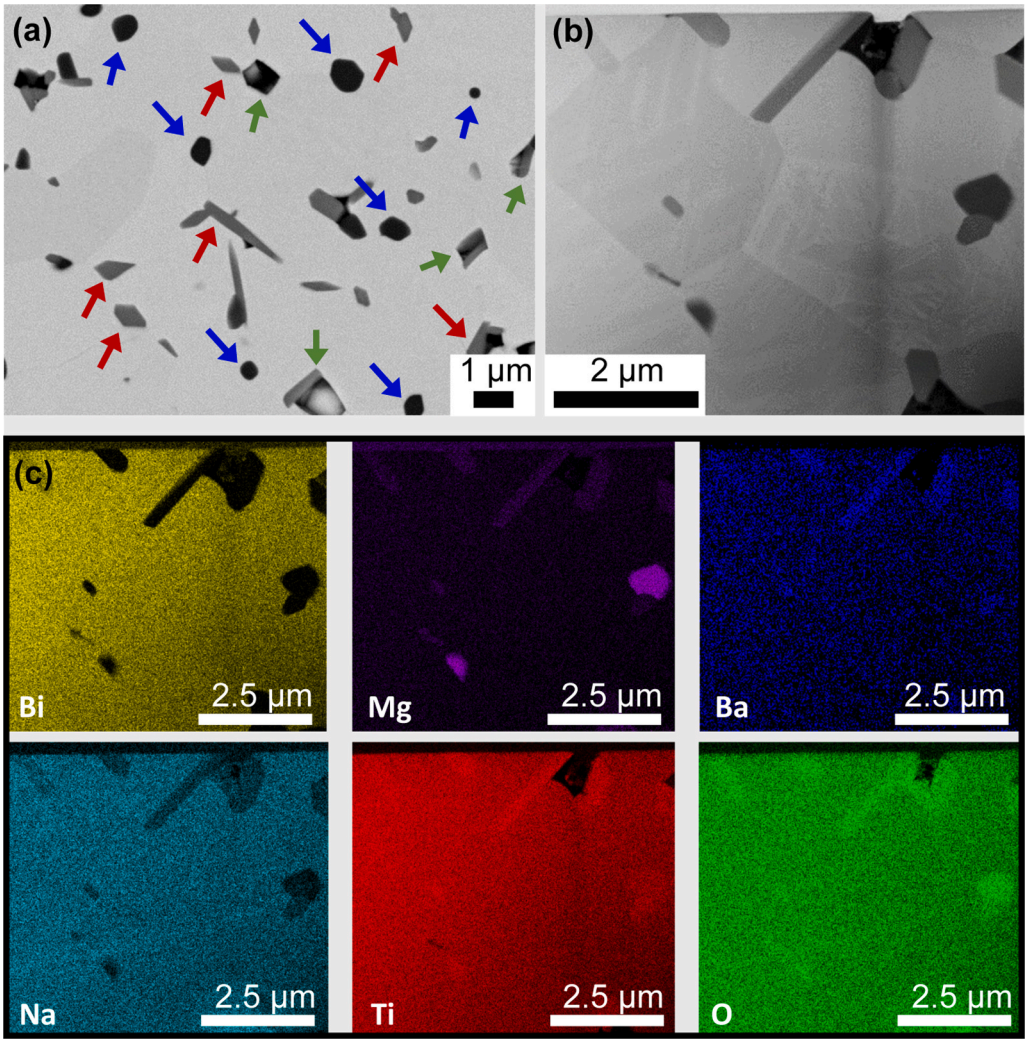

Fig. 5. BSE-SEM (a), BF-TEM (b) micrographs and EDX (c) evaluation of quenched NBT-BT-4$MgTiO_3$. (Color of arrows in (a): green - pores, blue - Mg-rich secondary phase; red - Ba-rich secondary phase).

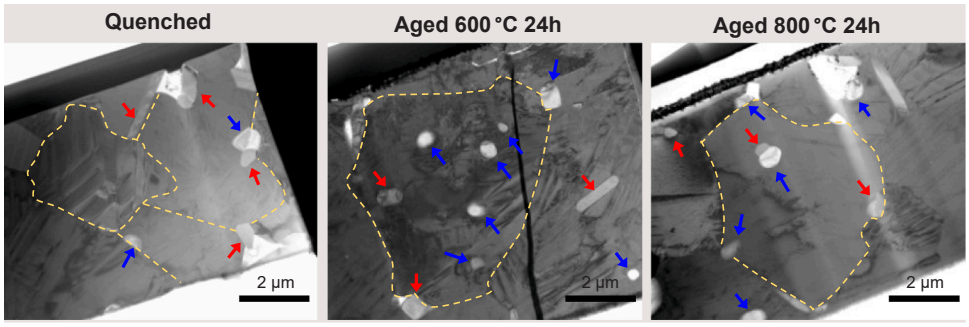

Fig. 6. TEM images of quenched and aged samples, where a dotted yellow line better visualizes grain boundaries, the Mg-rich precipitates are indicated by blue and Ba-rich secondary phase by red arrows.

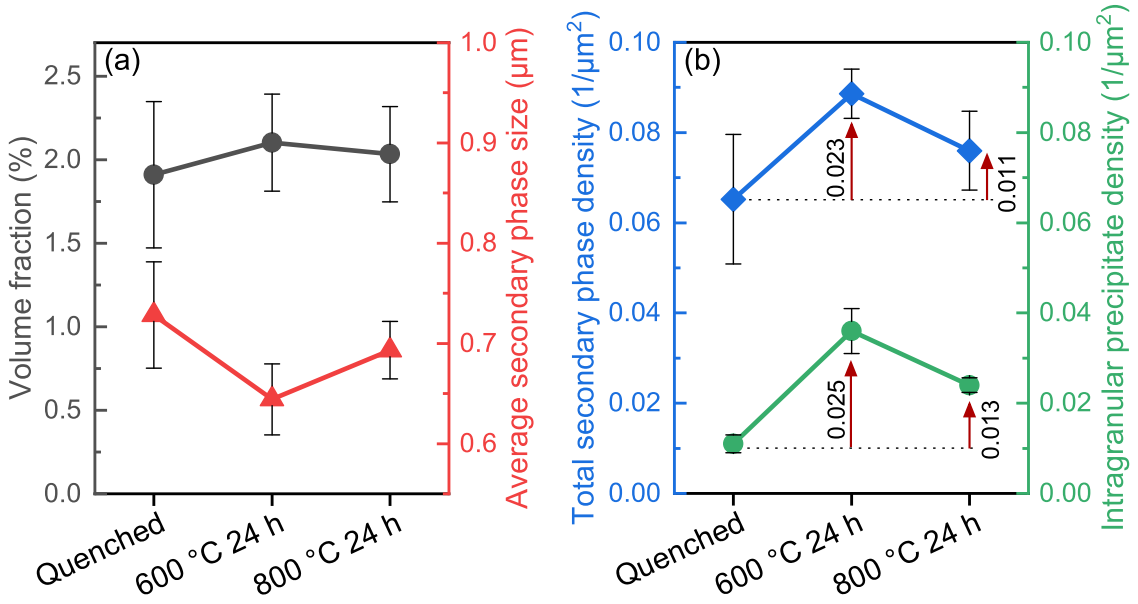

Fig. 7. Statistical analysis of Mg-rich secondary phases determined with SEM of quenched and aged samples, including in (a) the volume fraction and average size of secondary phases located inside the grain and at the grain boundary. In (b) the total secondary phase density of inter- and intragranular secondary phases and the intragranular precipitate density are displayed. Red errors indicate the absolute change in respective density due to aging.

The volume fraction of Mg-rich secondary phases in all samples is determined to be about 2 vol%. The substitution of NBT-BT with 4 mol% $MgTiO_3$ coincides here with 4 vol% of $MgTiO_3$ under the condition of no solubility. This implies that $MgTiO_3$ has been partially dissolved in the matrix. In aged samples, the volume fraction of Mg-rich phase demonstrates only a slight increase, while the average size of secondary phases, including both inter- and intragranular phases, decreases. This reduction in average size likely reflects the formation of smaller secondary phase particles induced by aging. This suggests that precipitation is promoted by aging. The tangible impact of aging on changes in the total density of secondary phases was further assessed by quantifying the number of intragranular and intergranular secondary phases per unit area, as depicted in Fig. 7(b). The findings indicate an increased density of secondary phases after aging, confirming that a greater number of smaller precipitates are formed. This rise in secondary phase density may account for the relatively slight change in volume fraction observed, as a reduction in the individual phase size balances the increase in phase quantity. Fig. 7(b) also presents the density of intragranular precipitates for both quenched and aged samples, demonstrating a pronounced increase in these types of precipitates with aging. The absolute enhancement of the intragranular precipitate density follows the same trend as the total secondary phase density, suggesting that the rise is primarily driven by the formation of intragranular precipitates rather than intergranular precipitates.

As precipitation results from reduced solubility with decreasing temperature, aging temperature influences both the nucleation and the growth of precipitates. A lower aging temperature should result in a more significant driving force for precipitation due to the larger difference between the solubility and the actual solute concentration [26,56]. Consistent with this premise, the sample aged at 600 °C for 24 h exhibits stronger precipitation, indicating a reduction in $MgTiO_3$ solubility with decreasing temperature. Additionally, precipitation predominantly occurs within the grains, implying a preference for homogeneous nucleation.

The sample aged at 800 °C for 24 h exhibits a larger average size and lower total number density of the secondary phase compared to those aged at a lower temperature. Precipitate coarsening is associated with the difference in solute concentration, the decrease of interfacial energy and thermally activated diffusion [34,57]. Hence, it is expected that higher aging temperature promotes precipitate growth. In addition to growth, the lower driving force for precipitation at higher aging temperature is due to the difference in solubility and actual solute concentration, which are plausible reasons. Therefore, a reduced density of precipitates at higher aging temperatures is obtained.

3.3. Properties

According to Zhao *et al.* [26,27], the introduction of intragranular precipitates alters domain structure and pins domain walls more effectively than intergranular secondary phases, thereby enhancing Q_m. The observed precipitation upon aging implies that these intragranular precipitates act as pinning sites for domain walls, potentially leading to ferroelectric hardening [58]. This effect is particularly expected in samples aged at 600 °C for 24 h, where the higher density of intragranular precipitates likely results in stronger ferroelectric hardening compared to both quenched samples and those aged at 800 °C, due to the greater number of pinning sites.

Fig. 8 displays polarization and strain behavior under large electric field of pure NBT-6BT and quenched and aged $MgTiO_3$-substituted NBT-BT. For the $MgTiO_3$-substituted samples, polarization saturation is reached at 7 kV/mm, while in the pure NBT-6BT sample saturation occurs at 6 kV/mm. $MgTiO_3$ substitution allows for higher field application and delayed polarization saturation compared to pure NBT-6BT. Upon first poling, NBT-BT undergoes an irreversible phase transition from a short-range relaxor to a long-range ferroelectric state, at the so-called initial poling field E_{pol}. All tested compositions exhibit characteristic butterfly- and square-shaped strain- and polarization-electric field hysteresis loops of a ferroelectric after the application of the initial poling field. $MgTiO_3$ substitution increases both the E_{pol} and the coercive field E_c, while reducing the remanent polarization P_r compared to pure NBT-BT, as exhibited in Table 1. This behavior indicates ferroelectric hardening caused by the precipitation hardening. However, the hardening arising from intergranular Ba- and Mg-rich phases has to be also considered, as it is observed in composite NBT-BT:ZnO [24]. The poling strain S_{pol}, which includes contributions from both domain switching and phase transformation during poling [59], is reduced for $MgTiO_3$-substituted NBT-BT. At the same time the irreversible poling strain, defined as the difference between zero strain at zero field to S_{neg} 1st loop and associated with phase transformation, is enhanced with the exception of the quenched sample. The enhancement is likely due to either a larger phase transformation strain from relaxor to ferroelectric phases, and/or a smaller reversible domain switching strain [60]. A similar effect has been observed for Mg-doped NBT-6BT [17]. Quenched samples may demonstrate different behavior because quenching can lead to spontaneous relaxor to ferroelectric transition in the absence of an external field [53]. Thus, the field-induced phase transition in the quenched sample is lower. According to Venkataraman *et al.* [55], annealing a quenched NBT-6BT sample at 800 °C abolishes the quenching effect, suggesting aging temperature mitigates or eliminates the quenching-induced phase transition. Negative strain, which is related to non-180° domain wall switching [61], decreases by the substitution of $MgTiO_3$ (Fig. 8(d)). This implies reduced ferroelectric-ferroelastic contribution, i.e. less non-180° domain wall motion [62]. The decrease in non-180° domain wall mobility is further confirmed by the reduction in d_{33} values (Table 1), as piezoelectric response is influenced by both intrinsic (lattice distortion) and extrinsic (non-180° domain wall motion) contributions [63]. This further

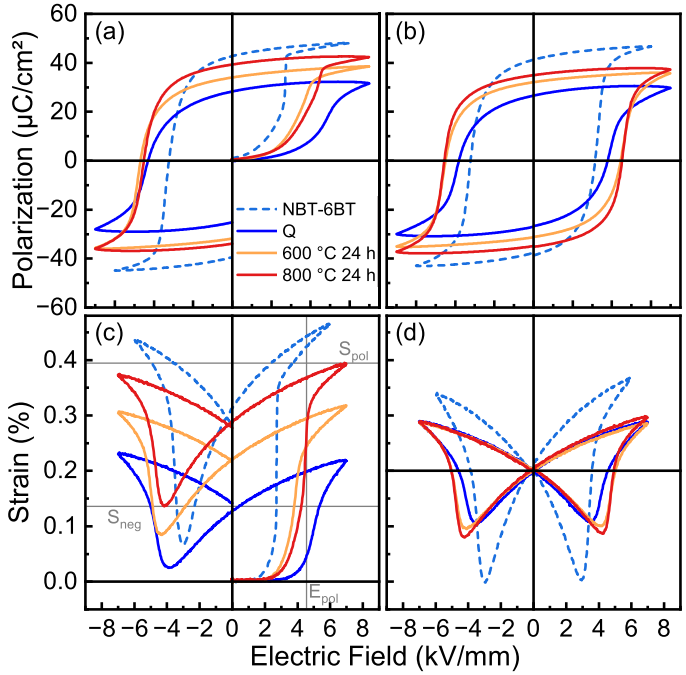

Fig. 8. Polarization-electric field hysteresis loops of 1st (a) and 3rd cycle (b). Strain-electric field hysteresis loops of 1st (c) and 3rd cycle (d). Exemplary for the aged sample at 800 °C S_{pol}, S_{neg} and E_{pol} are indicated by lines in (c).

Table 1
Summary of small- and large signal electromechanical properties of quenched and aged NBT-BT-$MgTiO_3$, including coercive field (E_c), poling field (E_{pol}) and remanent polarization (P_r), extracted from Fig. 8, piezoelectric constant d_{33} and planar mechanical quality factor (Q_m). Also, the grain size and transition temperature T_{F-R} are included, extracted from SEM and temperature-dependent permittivity measurements, respectively.

	E_c (kV/mm)	E_{pol} (kV/mm)	P_r (μC/cm²)	d_{33} (pC/N)	Q_m (-)	Grain size (μm)	T_{F-R} (°C)
NBT−6BT	3.1	2.7	41.3	140	138	1.2 ± 0.6	107
Quenched	3.7	5.1	28.0	85	435	3.4 ± 1.6	133
600 °C 24 h	4.4	4.1	32.1	86	564	3.5 ± 1.6	140
800 °C 24 h	4.5	4.5	36.8	94	505	3.7 ± 1.7	110

supports the role of $MgTiO_3$ substitution in promoting ferroelectric hardening.

Comparing quenched and aged compositions, E_c increases from 3.7 kV/mm for the quenched samples up to 4.5 kV/mm after aging. Extended aging at elevated temperature can also induce grain growth and bismuth evaporation, considering the volatility of bismuth [64], altering the microstructure and stoichiometry. The formation of precipitation reduces the amount of $MgTiO_3$ in the matrix compared to a quenched sample. Consequently, for changes in properties of aged samples, microstructural and compositional changes as well as the impact of the precipitates on the domain wall motion have to be considered. Grain size increases slightly during the aging process (Table 1). This minor variation, for example, result sample placement in the furnace. Hence, the increase is considered too small to significantly influence the properties. Bi-deficiency in NBT-BT does not appear to increase E_c as reported in prior study [65]. A lower $MgTiO_3$ content possibly leads to lower E_c, as observed in Mg-doped NBT-BT [17]. Therefore, this increase is most probable due to the greater density of intragranular precipitates formed during aging compared to the quenched sample. Zhao *et al.* [26,27] demonstrated that formed intragranular precipitates can effectively pin domain walls via lattice misfit-induced strains. The benefit of intragranular secondary phases is that the lattice-induced stresses are in closer proximity to domain walls, providing greater interaction with domain walls and therefore stronger pinning effects than intergranular phases. Therefore, higher electric fields are required to initiate domain switching in comparison to quenched samples. Aging enhances ferroelectric hardening, compounding the hardening effect initially introduced by $MgTiO_3$ substitution and secondary phase hardening. Although E_c remains comparable for samples aged at 600 °C and 800 °C, the sample aged at 800 °C exhibits higher P_r, negative strain as well as d_{33} values (Table 1). This suggests that aging at higher temperature intensifies domain wall mobility due to the lower density of intragranular precipitates.

Fig. 9 displays the mechanical quality factor Q_m and piezoelectric coefficient d_{33} for NBT-6BT, quenched and aged samples of $MgTiO_3$-substituted NBT-6BT. $MgTiO_3$ substitution leads to a significant increase of Q_m compared to NBT-6BT, with a 200 % rise observed between NBT-6BT and quenched NBT-6BT-4$MgTiO_3$. This is consistent with the observed ferroelectric hardening effect from $MgTiO_3$ substitution, as reflected in polarization and strain versus electric field loops. The increase in Q_m most likely arises from stress-induced domain wall pinning caused by intergranular Mg-rich and Ba-rich phases in the quenched sample. This is similar to the NBT-BT:ZnO composite system, where ZnO inclusions are predominantly located at grain boundaries [21,24]. Nonetheless, doping with Mg at the B-site can enhance the Q_m as well.

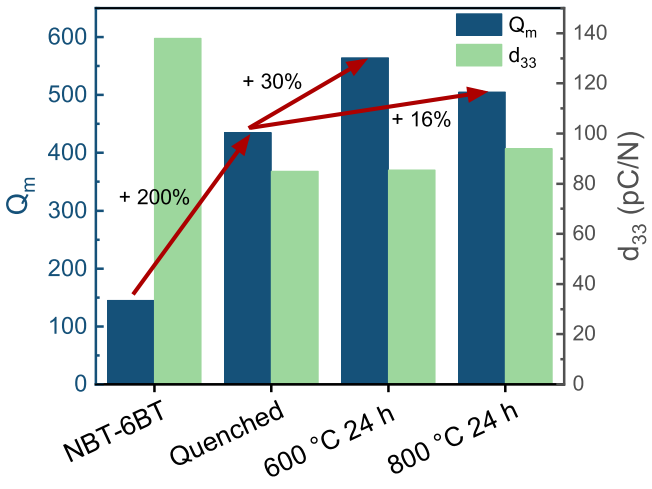

Fig. 9. Piezoelectric coefficient d_{33} and planar mechanical quality factor Q_m, of reference pure NBT-6BT, quenched and aged NBT-6BT-4$MgTiO_3$.

This should be considered as an additional contribution, given that 0.5 mol% Mg-doped NBT-6BT is reported to demonstrate a Q_m of up to 826 [17]. An increase due to quenching can be excluded, as only minor increases are reported from quenching NBT-6BT [55]. Additionally, it is not expected that the observed hardening stems from the grain size increase caused by $MgTiO_3$ substitution, as grain size effects on piezoelectric responses are mainly attributed to modifications in domain configurations, which seem to be most significant in the submicron grain size range [66,67]. Therefore, the influence of the grain size increase is considered minor compared to more dominant effects of potential Mg doping and precipitation hardening. While Q_m increases, d_{33} decreases with $MgTiO_3$ substitution. This known trade-off between Q_m and d_{33} is caused by the fact that reduced domain wall motion simultaneously lowers the extrinsic contribution to d_{33} [2,63].

Aging further improves Q_m compared to the quenched sample, while d_{33} remains comparable, diverging from the typical Q_m-d_{33} trade-off [2]. An increase in Q_m by Bi evaporation can be excluded, as only small changes in Q_m have been observed in a control experiment, where undoped NBT-6BT has been aged at 800°C. As discussed above, the enhancement is probably related to the formation of intragranular precipitates during aging. Namely, lower losses associated with domain wall motion and consequently increase Q_m are achieved by aging NBT-6BT-4$MgTiO_3$. Samples aged at 600 °C exhibit a 30 % increase, while samples aged at 800 °C only a 16 % increase in Q_m compared to the quenched sample. This fits well with the fact that more intragranular precipitates are formed at a lower temperature, since more sites for pinning domain walls and, therefore, higher Q_m. The distribution of the formed precipitates inside the grain seems to play a major role in pinning the domain walls, as the samples aged at 600 °C exhibit smaller precipitates but a greater density and, therefore, more pinning sites exist in the proximity of the domain walls. Hence, precipitate distribution is more important than the local volume fraction and size for the ferroelectric hardening.

Ferroelectric-relaxor transition temperature $T_{F\text{-}R}$ for NBT-6BT, quenched and aged samples of $MgTiO_3$-substituted NBT-6BT are listed in Table 1. Compared to NBT-6BT, $T_{F\text{-}R}$ is higher at 133°C for the quenched NBT-6BT-4$MgTiO_3$. An increase in transition temperature implies an enhanced stabilization of the ferroelectric long-range order [53,68]. As previously discussed, quenching induces a more pronounced rhombohedral distortion, indicating a stabilization of the ferroelectric order and elevating $T_{F\text{-}R}$ [54]. Besides quenching, both acceptor-doped and secondary phase hardening are also reported to increase $T_{F\text{-}R}$. Acceptor doping achieves this by enhancing the tetragonal phase fraction and its lattice distortion, while the secondary phase hardening stabilizes the ferroelectric state via a stress-induced mechanism [17,21]. It is likely that the misfit stresses induced by the secondary phases influence the crystal distortion. However, distortions caused by secondary phases might be more localized and too subtle to be reliably detected by lab-scale XRD [69,70]. Hence, the observed rhombohedral distortion in the quenched and 600 °C aged sample (Fig. 4) results predominantly from quenching. An increase in the grain size is reported to increase the depolarization temperature, which is assigned to higher ferroelectric ordering [51]. Nevertheless, in this case, the effect of quenching is considered more dominant, as no significant grain size variation is observed between quenched and aged samples. Therefore, the higher $T_{F\text{-}R}$ in quenched samples compared to pure NBT-BT is likely the result of a combined effect of quenching and secondary phase hardening from intergranular secondary phases. However, the precise justification for this increase in transition temperature cannot be fully clarified, for example, information on lattice distortion and phase fractions (rhombohedral, tetragonal, cubic) of the poled sample were not investigated. Samples aged at 600°C for 24 h exhibit a $T_{F\text{-}R}$ of 140 °C, whereas aging at 800 °C reduces $T_{F\text{-}R}$ to 110 °C. Previous studies report that annealing quenched NBT-BT at 800 °C for 12 h reverses the quenched state [55], which aligns with the observed pseudocubic structure in the 800 °C aged samples. This suggests that samples aged at 800 °C likely no longer

benefit from quenching, resulting in a lower T_{F-R}. In contrast, the lower aging temperature does not reverse the quenching effect, preserving the contribution of quenching to T_{F-R}. Notably, the T_{F-R} of the 600 °C aged samples exceeds that of quenched samples, suggesting an additional contribution from intragranular precipitates to the depolarization temperature. These precipitates may induce internal stresses within the grains, further stabilize the ferroelectric state, albeit to a lesser extent than quenching.

4. Conclusion

An empirical approach, based on evaluating the ionic radii and tolerance factor of potential third members in NBT-BT and their correlation with structural compatibility in perovskite-structured NBT-BT, led to the selection of $MgTiO_3$ as a suitable substitute. Thermal analysis and ex-situ XRD evaluation indicate that $MgTiO_3$ substitution does not significantly alter the calcination process. In contrast to the expectation to achieve a secondary phase-free microstructure for sintered and subsequently quenched samples, SEM and TEM reveal Mg- and Ba-rich intergranular secondary phases. Hence, substitution of $MgTiO_3$ in NBT-6BT promotes secondary phase hardening, indicated by the 200 % increase in Q_m in quenched samples. Aging treatments on quenched samples initiate precipitation of small Mg-rich intragranular secondary phases. These serve as additional domain wall pinning sites to already intergranular secondary phases in a quenched sample, suppressing domain wall motion effectively due to misfit-induced stresses by formed precipitates in the close proximity of domain walls, thereby increasing Q_m. The observed increase of 30 % in Q_m and 19 % in E_c, and decreased P_r, negative strain and d_{33} compared to quenched samples are directly linked to the formation of intragranular precipitates. Notably, samples aged at lower aging temperatures exhibit a stronger hardening effect due to the greater density of precipitates, highlighting the importance of precipitate distribution over their size and volume fraction. The results demonstrate that precipitation hardening is a viable approach for ferroelectric hardening in NBT-based piezoceramics, effectively reducing mechanical losses in high-power applications. Furthermore, it proves that the concept of precipitation hardening is also applicable in relaxor ferroelectrics, expanding its potential for material optimization. However, achieving complete solubility of $MgTiO_3$ after quenching still remains a challenge.

CRediT authorship contribution statement

Friederike Aßmann: Resources, Conceptualization. **Tanja Einhellinger-Müller:** Resources, Conceptualization. **Siegfried Teuber:** Investigation. **Sabrina Kahse:** Writing – review & editing, Writing – original draft, Visualization, Investigation, Formal analysis, Conceptualization. **Florian Schönhöfer:** Resources, Conceptualization. **Lovro Fulanovic:** Writing – review & editing, Supervision, Conceptualization. **Sebastian Zischke:** Investigation. **Jürgen Rödel:** Writing – review & editing, Supervision, Conceptualization.

Declaration of Competing Interest

The authors declare that they have no known competing financial interests or personal relationships that could have appeared to influence the work reported in this paper.

Acknowledgement

The authors thank CeramTec GmbH for generous financial support. Marc Widenmeyer is acknowledged for support with TGA/DTA measurements.

References

[1] K. Uchino, Piezoelectric devices in the sustainable society, Sustain. Environ. 4 (4) (2019) p181, https://doi.org/10.22158/se.v4n4p181.
[2] S. Zhang, R. Xia, L. Lebrun, D. Anderson, T.R. Shrout, Piezoelectric materials for high power, high temperature applications, Mater. Lett. 59 (27) (2005) 3471–3475, https://doi.org/10.1016/j.matlet.2005.06.016.
[3] T.N. Nguyen, et al., Hardening effect in lead-free piezoelectric ceramics, J. Mater. Res. 36 (5) (2021) 996–1014, https://doi.org/10.1557/s43578-020-00016-1.
[4] G. Liu, S. Zhang, W. Jiang, W. Cao, Losses in ferroelectric materials, Elsevier Ltd (2015), https://doi.org/10.1016/j.mser.2015.01.002.
[5] D. Damjanovic, Contributions to the piezoelectric effect in ferroelectric single crystals and ceramics, J. Am. Ceram. Soc. 88 (10) (2005) 2663–2676, https://doi.org/10.1111/j.1551-2916.2005.00671.x.
[6] K. Uchino, et al., Loss mechanisms and high power piezoelectrics, J. Mater. Sci. 41 (1) (2006) 217–228, https://doi.org/10.1007/s10853-005-7201-0.
[7] M. Hejazi, E. Taghaddos, E. Gurdal, K. Uchino, A. Safari, High power performance of Manganese-Doped BNT-Based Pb-Free piezoelectric ceramics, J. Am. Ceram. Soc. 97 (10) (2014) 3192–3196, https://doi.org/10.1111/jace.13098.
[8] B. Jaffe, W.R. Cook, H. Jaffe, Piezoelectric Ceramics, Academic Press, 1971.
[9] A.J. Bell, O. Deubzer, Lead-free piezoelectrics - the environmental and regulatory issues, MRS Bull. 43 (8) (2018) 581–587, https://doi.org/10.1557/mrs.2018.154.
[10] T. Takenaka, K. Maruyama, K. Sakata, $Bi_{1/2}Na_{1/2})TiO_3$-$BaTiO_3$ system for lead-free piezoelectric ceramics, Jpn. J. Appl. Phys. 30 (9B) (1991) 2236–2239.
[11] A.R. Paterson, et al., Relaxor-ferroelectric transitions: sodium bismuth titanate derivatives, Aug. 01, Cambridge University Press, 2018, https://doi.org/10.1557/mrs.2018.156.
[12] Y. Hiruma, T. Watanabe, H. Nagata, T. Takenaka, Piezoelectric properties of $(Bi_{1/2}Na_{1/2})TiO_3$–$BaTiO_3$-based solid solution for lead-free high-power applications, Jpn. J. Appl. Phys. 47 (9) (2008) 7659–7663, https://doi.org/10.1143/JJAP.47.7659.
[13] T. Tou, Y. Hamaguti, Y. Maida, H. Yamamori, K. Takahashi, Y. Terashima, Properties of $(Bi_{0.5}Na_{0.5})TiO_3$–$BaTiO_3$–$(Bi_{0.5}Na_{0.5})(Mn_{1/3}Nb_{2/3})O_3$ Lead-Free piezoelectric ceramics and its application to ultrasonic cleaner, PART 2, Jpn. J. Appl. Phys. 48 (7) (2009) 5–9, https://doi.org/10.1143/JJAP.48.07GM03.
[14] M. Slabki, K.V. Lalitha, J. Rödel, J. Koruza, Origin of high-power drive stability in $(Bi_{1/2}Na_{1/2})TiO_3$–$BaTiO_3$ based piezoceramics, Acta Mater. 227 (2022) 117703, https://doi.org/10.1016/j.actamat.2022.117703.
[15] C. Ma, H. Guo, S.P. Beckman, X. Tan, Creation and destruction of morphotropic phase boundaries through electrical poling: a case study of lead-free $(Bi_{1/2}Na_{1/2})TiO_3$–$BaTiO_3$ piezoelectrics, Phys. Rev. Lett. 109 (10) (2012) 107602, https://doi.org/10.1103/PhysRevLett.109.107602.
[16] C. Xu, D. Lin, K.W. Kwok, Structure, electrical properties and depolarization temperature of $(Bi_{0.5}Na_{0.5})TiO_3$-$BaTiO_3$ lead-free piezoelectric ceramics, Solid State Sci. 10 (7) (2008) 934–940, https://doi.org/10.1016/j.solidstatesciences.2007.11.003.
[17] D. Bremecker, M. Slabki, J. Koruza, J. Rödel, Characterization of crystal structure, electrical and electromechanical properties of Mg-doped $0.94Bi_{1/2}Na_{1/2}TiO_3$–$0.06BaTiO_3$, J. Eur. Ceram. Soc. 42 (13) (2022) 5591–5597, https://doi.org/10.1016/j.jeurceramsoc.2022.06.032.
[18] L. Chen, H. Liu, H. Qi, J. Chen, High-electromechanical performance for high-power piezoelectric applications: fundamental, progress, and perspective, Prog. Mater. Sci. 127 (2022) 100944, https://doi.org/10.1016/j.pmatsci.2022.100944.
[19] M.I. Morozov, D. Damjanovic, Charge migration in $Pb(Zr,Ti)O_3$ ceramics and its relation to ageing, hardening, and softening, J. Appl. Phys. 107 (3) (2010), https://doi.org/10.1063/1.3284954.
[20] J. Zhang, et al., Semiconductor/relaxor 0-3 type composites without thermal depolarization in $Bi_{0.5}Na_{0.5}TiO_3$-based lead-free piezoceramics, Nat. Commun. 6 (1) (2015) 6615, https://doi.org/10.1038/ncomms7615.
[21] L.M. Riemer, et al., Stress-induced phase transition in lead-free relaxor ferroelectric composites, Acta Mater. 136 (2017) 271–280, https://doi.org/10.1016/j.actamat.2017.07.008.
[22] M. Slabki, L.K. Venkataraman, T. Rojac, J. Rödel, J. Koruza, Thermal stability of the electromechanical properties in acceptor-doped and composite-hardened $(Bi_{1/2}Na_{1/2})TiO_3$–$BaTiO_3$ ferroelectrics, J. Appl. Phys. 130 (1) (2021), https://doi.org/10.1063/5.0052293.
[23] L. K. V, et al., Spontaneous ferroelectric order in lead-free relaxor $Na_{1/2}Bi_{1/2}TiO_3$-based composites, Phys. Rev. B 101 (17) (2020) 174108, https://doi.org/10.1103/PhysRevB.101.174108.
[24] K.V. Lalitha, L.M. Riemer, J. Koruza, J. Rödel, Hardening of electromechanical properties in piezoceramics using a composite approach, Appl. Phys. Lett. 111 (2) (2017) 1–6, https://doi.org/10.1063/1.4986911.
[25] L. Kodumudi Venkataraman, T. Frömling, J. Rödel, Role of matrix phase and electric field gradient in $Na_{1/2}Bi_{1/2}TiO_3$:ZnO composites, J. Mater. 8 (2) (2022) 498–510, https://doi.org/10.1016/j.jmat.2021.06.008.
[26] C. Zhao, et al., Precipitation hardening in ferroelectric ceramics, Adv. Mater. 33 (36) (2021) 2102421, https://doi.org/10.1002/adma.202102421.
[27] C. Zhao, S. Gao, H.J. Kleebe, X. Tan, J. Koruza, J. Rödel, Coherent precipitates with strong domain wall pinning in alkaline niobate ferroelectrics, Adv. Mater. 34 (38) (2022) 2202379, https://doi.org/10.1002/adma.202202379.
[28] J.E. Daniels, W. Jo, J. Rödel, J.L. Jones, Electric-field-induced phase transformation at a lead-free morphotropic phase boundary: case study in a 93% $(Bi_{0.5}Na_{0.5})TiO_3$-7% $BaTiO_3$ piezoelectric ceramic, Appl. Phys. Lett. 95 (3) (2009) 2007–2010, https://doi.org/10.1063/1.3182679.
[29] Y. Zhang, et al., Phase-transition induced optimization of electrostrain, electrocaloric refrigeration and energy storage of $LiNbO_3$ doped BNT-BT ceramics,

Ceram. Int. 46 (2) (2020) 1343–1351, https://doi.org/10.1016/j.ceramint.2019.09.097.
[30] Y. Li, et al., Large strain response and Fatigue-Resistant behavior in ternary $Bi_{0.5}Na_{0.5}TiO_3$–$BaTiO_3$–$Bi(Zn_{0.5}Ti_{0.5})O_3$ solid solutions, J. Am. Ceram. Soc. 97 (11) (2014) 3615–3623, https://doi.org/10.1111/jace.13176.
[31] L. Wang, et al., Tailoring electromechanical performance in $BiScO_3$-modified $Bi_{0.5}Na_{0.5}TiO_3$-based lead-free piezoceramics, J. Mater. Sci. 31 (2020) 1491–1501.
[32] European Committee for Electrotechnical Standardization, Piezoelectric properties of ceramic materials and components-Part 2: Methods of measurement–Low power (EN 50324-2), 2002.
[33] T. Gladman, Precipitation hardening in metals, Mater. Sci. Technol. 15 (1) (1999) 30–36, https://doi.org/10.1179/026708399773002782.
[34] Z. Guo, W. Sha, Quantification of precipitation hardening and evolution of precipitates, Mater. Trans. 43 (6) (2002) 1273–1282, https://doi.org/10.2320/matertrans.43.1273.
[35] V.M. Goldschmidt, Die gesetze der krystallochemie, Naturwissenschaften 14 (21) (1926) 477–485.
[36] R.D. Shannon, Revised effective ionic radii and systematic studies of interatomie distances in halides and chaleogenides, Acta Crystallogr. Sect. A 32 (5) (1976) 751–767.
[37] G. Liu, et al., Phase segregation and dielectric, ferroelectric, and piezoelectric properties of MgO-doped NBT-BT lead-free ferroelecric ceramics, Mater. Res. Express 5 (3) (2018), https://doi.org/10.1088/2053-1591/aab33b.
[38] J. Yang, P. Ren, X. Wang, G. Wang, L. Lu, Effect of quenching treatment on photochromic properties of Mg^{2+} doped $Na_{1/2}Bi_{1/2}TiO_3$ ceramics, J. Eur. Ceram. Soc. 43 (11) (2023) 4782–4790, https://doi.org/10.1016/j.jeurceramsoc.2023.04.048.
[39] K. Sreedhar, N. Pavaskar, Synthesis of $MgTiO_3$ and $Mg_4Nb_2O_9$ using stoichiometrically excess MgO, Mater. Lett. 53 (6) (2002) 452–455, https://doi.org/10.1111/j.1744-7402.2007.02151.x.
[40] B. Tang, S. Zhang, X. Zhou, C. Deng, S. Yu, Preparation of pure $MgTiO_3$ powders and the effect of the $ZnNb_2O_6$-dope onto the property of $MgTiO_3$-based ceramics, J. Alloy. Compd. 492 (1–2) (2010) 461–465, https://doi.org/10.1016/j.jallcom.2009.11.140.
[41] Inorganic Crystal Structure Database (ICSD), FIZ Karlsruhe
[42] J. Zhao, et al., Polar domain structural evolution under electric field and temperature in the $(Na_{0.5}Bi_{0.5})TiO_3$-0.06$BaTiO_3$ piezoceramics, J. Am. Ceram. Soc. 102 (1) (2019) 437–447, https://doi.org/10.1111/jace.15883.
[43] D. Hou, et al., Formation of sodium bismuth titanate—barium titanate during solid-state synthesis, J. Am. Ceram. Soc. 100 (4) (2017) 1330–1338, https://doi.org/10.1111/jace.14631.
[44] E. Aksel, J.L. Jones, Phase formation of sodium bismuth titanate perovskite during solid-state processing, J. Am. Ceram. Soc. 93 (10) (2010) 3012–3016, https://doi.org/10.1111/j.1551-2916.2010.03977.x.
[45] M.I. Morozov, L.P. Mezentseva, V.V. Gusarov, Mechanism of formation of $Bi_4Ti_3O_{12}$, Russ. J. Gen. Chem. 72 (7) (2002) 1038–1040, https://doi.org/10.1023/A:1020734312307.
[46] M.J. Harris, E.K.H. Salje, The incommensurate phase of sodium carbonate: an infrared absorption study, J. Phys. Condens. Matter 4 (18) (1992) 4399–4408, https://doi.org/10.1088/0953-8984/4/18/007.
[47] G. Esteves, C.M. Fancher, J.L. Jones, In situ characterization of polycrystalline ferroelectrics using X-ray and neutron diffraction, J. Mater. Res. 30 (3) (2015) 340–356, https://doi.org/10.1557/jmr.2014.302.
[48] I.P. Swainson, M.T. Dove, M.J. Harris, Neutron powder diffraction study of the ferroelastic phase transition and lattice melting in sodium carbonate, Na_2CO_3, J. Phys. Condens. Matter 7 (23) (1995) 4395–4417, https://doi.org/10.1088/0953-8984/7/23/010.
[49] L. Zevin, G. Kimmel, Quantitative X-Ray Diffractometry, Springer, 1995.
[50] A.K. Fetzer, A. Wohninsland, K. Hofmann, O. Clemens, L. Kodumudi Venkataraman, H.J. Kleebe, Domain structure and phase evolution in quenched and furnace cooled lead-free $Na_{1/2}Bi_{1/2}TiO_3$ ceramics, Open Ceram. 5 (Mar. 2021) 100077, https://doi.org/10.1016/j.oceram.2021.100077.
[51] D.K. Khatua, et al., A coupled microstructural-structural mechanism governing thermal depolarization delay in $Na_{0.5}Bi_{0.5}TiO_3$-based piezoelectrics, Acta Mater. 179 (Oct. 2019) 49–60, https://doi.org/10.1016/j.actamat.2019.08.022.
[52] A. Wohninsland, A.K. Fetzer, R. Broughton, J.L. Jones, K.V. Lalitha, Structural and microstructural description of relaxor-ferroelectric transition in quenched $Na_{1/2}Bi_{1/2}TiO_3$–$BaTiO_3$, J. Mater. 8 (4) (2022) 823–832, https://doi.org/10.1016/j.jmat.2022.01.006.
[53] K.V. Lalitha, J. Koruza, J. Rödel, Propensity for spontaneous relaxor-ferroelectric transition in quenched $(Na_{1/2}Bi_{1/2})TiO_3$, Appl. Phys. Lett. 113 (25) (2018), https://doi.org/10.1063/1.5053989.
[54] H. Nagata, Y. Takagi, Y. Yoneda, T. Takenaka, Correlation between depolarization temperature and lattice distortion in quenched $(Bi_{1/2}Na_{1/2})TiO_3$-based ceramics, Appl. Phys. Express 13 (6) (2020), https://doi.org/10.35848/1882-0786/ab8c1d.
[55] L.K. Venkataraman, Influence of quenching and subsequent annealing on the conductivity and electromechanical properties of $Na_{1/2}Bi_{1/2}TiO_3$, Materials 14 (9) (2021) 2149, https://doi.org/10.3390/ma14092149.
[56] D.A. Porter, K.E. Easterling, M.Y. Sherif. Phase Transformations in Metals and Alloys (Revised Reprint), 3rd ed., CRC Press, 2009.
[57] J.W. Martin. Precipitation Hardening: Theory and Applications, 2nd ed., Butterworth-Heinemann, 1998.
[58] O. Taylor, E. Chaffee, X. Tian, C. Zhao, L. Zhou, X. Tan, $CaTiO_3$-rich precipitates and their impacts on ferroelectric domains during heating in (Ba,Ca)TiO_3 ceramics, J. Mater. Sci. Mater. Electron 35 (27) (2024) 1–9, https://doi.org/10.1007/s10854-024-13530-3.
[59] N.H. Khansur, M. Hinterstein, Z. Wang, C. Groh, W. Jo, J.E. Daniels, Electric-field-induced strain contributions in morphotropic phase boundary composition of $(Bi_{1/2}Na_{1/2})TiO_3$-$BaTiO_3$ during poling, Appl. Phys. Lett. 107 (24) (2015), https://doi.org/10.1063/1.4937470.
[60] W. Jo, J. Rödel, Electric-field-induced volume change and room temperature phase stability of $(Na_{1/2}Bi_{1/2})TiO_3$-x mol.% $BaTiO_3$ piezoceramics, Appl. Phys. Lett. 99 (4) (2011) 0–3, https://doi.org/10.1063/1.3615675.
[61] T. Tsurumi, Y. Kumano, N. Ohashi, T. Takenaka, O. Fukunaga, 90° domain reorientation and electric-field-induced strain of tetragonal lead zirconate titanate ceramics, Jpn. J. Appl. Phys. Part 1 Regul. Pap. Short. Notes Rev. Pap. 36 (9. B) (1997) 5970–5975, https://doi.org/10.1143/jjap.36.5970.
[62] J. Schultheiß, et al., Revealing the sequence of switching mechanisms in polycrystalline ferroelectric/ferroelastic materials, Acta Mater. 157 (2018) 355–363, https://doi.org/10.1016/j.actamat.2018.07.018.
[63] D. Damjanovic, Ferroelectric, dielectric and piezoelectric properties of ferroelectric thin films and ceramics, Rep. Prog. Phys. 61 (11) (1998) 1267–1324, https://doi.org/10.1088/0034-4885/61/9/002.
[64] J. Carter, E. Aksel, T. Iamsasri, J.S. Forrester, J. Chen, J.L. Jones, Structure and ferroelectricity of nonstoichiometric $(Na_{0.5}Bi_{0.5})TiO_3$, Appl. Phys. Lett. 104 (11) (2014) 3–7, https://doi.org/10.1063/1.4868109.
[65] I.T. Seo, S. Steiner, T. Frömling, The effect of a site non-stoichiometry on 0.94 $(Na_yBi_x)TiO_3$-0.06$BaTiO_3$, J. Eur. Ceram. Soc. 37 (4) (2017) 1429–1436, https://doi.org/10.1016/j.jeurceramsoc.2016.11.045.
[66] D.K. Khatua, T. Mehrotra, A. Mishra, B. Majumdar, A. Senyshyn, R. Ranjan, Anomalous influence of grain size on the global structure, ferroelectric and piezoelectric response of $Na_{0.5}Bi_{0.5}TiO_3$, Acta Mater. 134 (2017) 177–187, https://doi.org/10.1016/j.actamat.2017.05.068.
[67] X. Liu, S. Xue, F. Wang, J. Zhai, B. Shen, Grain size dependent physical properties in lead-free multifunctional piezoceramics: a case study of NBT-xST system, Acta Mater. 164 (2019) 12–24, https://doi.org/10.1016/j.actamat.2018.10.029.
[68] K.V. Lalitha, B. Wang, P. Ren, D.A. Hall, T. Rojac, Quenching effects and mechanisms in bismuth-based perovskite ferroelectrics, Open Ceram. 10 (2022) 100259, https://doi.org/10.1016/j.oceram.2022.100259.
[69] R. Ranjan, A. Dviwedi, Structure and dielectric properties of $(Na_{0.50}Bi_{0.50})1$-xBa_xTiO_3: $0 \leq x \leq 0.10$, Solid State Commun. 135 (6) (2005) 394–399, https://doi.org/10.1016/j.ssc.2005.03.053.
[70] B.N. Rao, D.K. Khatua, R. Garg, A. Senyshyn, R. Ranjan, Structural crossover from nonmodulated to long-period modulated tetragonal phase and anomalous change in ferroelectric properties in the lead-free piezoelectric $Na_{1/2}Bi_{1/2}TiO_3$-$BaTiO_3$, Phys. Rev. B Condens. Matter Mater. Phys. 91 (21) (2015) 1–9, https://doi.org/10.1103/PhysRevB.91.214116.